ACS APPLIED MATERIALS & INTERFACES

Research Article

www.acsami.org

Low-Temperature Fabrication of Au–Co Cluster Mixed Nanohybrids With High Magnetic Moment of Co

Dong-Feng Zhang,[†] Qian Zhang,[†] Wei-Feng Huang,[§] Lin Guo,*[,†] Wei-Meng Chen,[‡] Wang-Sheng Chu,[§] Chinping Chen,*[,‡] and Zi-Yu Wu*[,§]

[†]School of Chemistry and Environment, Beihang University, Beijing 100191, PR China

[‡]Department of Physics, Peking University, Beijing 100871, PR China

[§]National Synchrotron Radiation Laboratory, University of Science and Technology of China, Hefei, Anhui 230029, PR China

Supporting Information

ABSTRACT: In recent years, the synergistic effects of Au-based hybrids have generated enormous scientific interest. The hybrids of Au and Co are expected to exhibit attractive properties. In this paper, we report the successful fabrication of the nanohybrids between bulk-immiscible Au and Co with chain-like structures via a mild solution method. Elemental mapping, XRD and EXAFS data reveal that the as-prepared AuCo nanohybrids might be of cluster mixed configuration. A sequential redox and imperfection-promoted aggregation/diffusion process is proposed to elucidate the formation mechanism of the nanohybrids. The as-prepared products exhibit a temperature-independent saturation magnetization with the magnetic moment of Co as high as ~2.95 μ_B for each Co atom at 300 K, much higher than the bulk value (~1.7 μ_B for each Co atom) and approaching the theoretical value of an atomic Co (~3.0 μ_B for each Co atom).

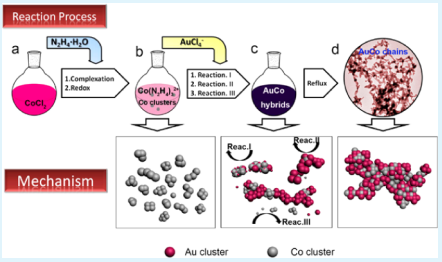

KEYWORDS: *Au–Co, bimetallic, nanohybrids, network-like, sequential redox, magnetic properties*

1. INTRODUCTION

To explore new materials with unique properties has been a great research motivation for chemists, physicists, and material scientists. In this regards, nanohybrids, with multiple components integrated into a single nanostructure, are important because of collected, enhanced, and/or possible new properties produced from synergistic effects.[1,2] Among various combinations, Au-based hybrids have attracted tremendous research interest. With high chemical stability and unique optical properties, integration with Au nanoparticles (NPs) can not only introduce plasmatic properties but also facilitate chemical functionalization to enhance solubility in various media and promote biocompatibility.[3−5] Enhanced and tunable optical and catalytic functions have been achieved in Au-based hybrid nanosystems originating from modified electronic structures due to interparticle charge transfer.[6−16] For example, the contact between Au nanoparticles (NPs) and metal oxides is found to impart "inert" Au with highly catalytic activity.[6−11] The formation of Au-semiconductor heterojunctions greatly enhances its light absorption and improves its photoconversion efficiency because of a fast charge-transfer process.[12−15] The alloying of less reactive Au with Pt or Pd could generate enhanced catalytic activity and selectivity, which have been used in various catalytic reaction including automobile catalytic converters.[17−21] The fabrication of Au-based hybrid nanocrystals is important to both the frontier of fundamental science and to the exploration of novel functional materials.

With the appealing magnetic and catalytic properties, cobalt nanoparticles hold promising applications in various fields, including magnetic resonance imaging, catalysts, drug delivery, and bioseparation.[22−25] The hybrids based on nanoscaled Au and Co are expected to exhibit more attractive properties because of the possible giant magnetoresistance (GMR) effect and the optical-magnetic bifunctionalities.[26,27] Furthermore, it would also create models for studying the coupling interactions between metals and their effects on physical and chemical properties. Y. D. Li's group reported that Au@Co core–shell nanostructures possess improved catalytic activity toward CO oxidation in comparison with the monometallic counterparts.[28] Xu and the cooperators's work also revealed Au@Co core–shell nanostructures exhibited high catalytic activity and long-term stability for the hydrolytic dehydrogenation of ammonia borane.[29] However, the limited literature mainly focused on the core–shell structures.[28−30] Because of the large miscibility gap, it is a challenge to synthesis atomic ordering or cluster mixed Au–Co nanohybrids.

Herein, we report the successful fabrications of component uniform distributed Au–Co network-like nanohybrids via a low temperature solution process. Elemental mapping profiles and EXAFS data suggest that the product were of cluster-mixed configuration. A sequential redox mechanism is proposed to

Received: August 6, 2012
Accepted: September 26, 2012
Published: September 26, 2012

illustrate the formation process. The as-prepared products exhibit a high magnetic moment for each Co atom, as high as ~2.95 μ_B for each Co atom, which is much higher than 1.7 μ_B for each Co atom of the bulk phase.

2. EXPERIMENTAL SECTION

2.1. Preparation of AuCo Nanohybrids. All reagents were used without further purification. Typically, $CoCl_2{\cdot}6H_2O$ (0.3032 g) and PVP (0.4260 g) were dissolved into 30.0 mL of ethylene glycol (EG) under constant stirring. After stirring for 2h, a homogeneous transparent mauve solution formed. Then, 1.5 mL $N_2H_4{\cdot}H_2O$ (50 vol%) was added drop by drop into the above solution, which made the solution become turbid and the color turn into pink. After reaction for 3 h, 53 mL EG solution of $HAuCl_4$ (4×10^{-3} mol·L^{-1}) was transferred into the above mixture and the color of the solution instantly changed into dark blue. After 0.5 h constant stirring, the temperature was raised to the boiling point (197 °C) and kept refluxing for 4 h. During the process, numerous bubbles were observed and an ammonia smell could be discerned. After the mixture was cooled to room temperature, the produced precipitates were collected by centrifugation and washed with ethanol several times. All the experimental procedures were performed open to the atmosphere.

2.2. Characterization. Transmission electron microscope (TEM) characterizations were carried out with JEOL 2100F microscope working at 200 kV. The X-ray diffraction (XRD) pattern was recorded on a powder sample with a Rigaku D/max-2200 diffractometer employing Cu K_α radiation (λ = 1.54056 Å) at a scanning rate of 0.02 deg/s ranging from 30 to 90°. X-ray absorption fine structure (XAFS) spectra monochromated by Si(111) double crystals were measured at the beamline U7C of National Synchrotron Radiation Facility (NSRL), China. The XAFS signal was collected in transmission mode and the data were analyzed by FEFE8 software packages. The magnetic properties of the sample were measured using a Quantum Design SQUID magnetometer.

3. RESULTS AND DISCUSSION

As revealed by the transmission electron microscope (TEM) observations (Figure 1a), the products exhibit as chain-like nanostructures with diameters ranging from 20 to 80 nm, which tend to cross-link into network structures. Elemental mapping (Figure 1c, d) reveals the uniform distribution of Au and Co. Energy-dispersive X-ray spectroscopy (EDS) data on large areas of the chains show that the average molar ratio of Au to Co approaches 1:1 (see Figure S1 in the Supporting Information).

Figure 2a–c shows the X-ray diffraction patterns of the nanohybrids, face-centered cubic (fcc) structured Co with JCPDS No. 01–1259, and fcc-Au with JCPDS No. 04–0784, respectively. It can be seen that the diffraction pattern of the product is similar to that of Au and no signal from Co can be identified. First-principle calculations suggested that for the bulk immiscible Co and Au, it is possible to form intermetallic compounds with metastable states of elastically stable fcc-type structures for Co:Au = 1:3, 1:1, and 3:1, with a slightly reduced lattice constant from that of Au fcc structure.[31] This is expected since the atomic diameter of Co is smaller than that of Au. In the present work, however, no diffraction peak shift can be identified, which excludes the possibility of the intermetallic structure of the nanohybrids. Recalling the uniform distribution of Au and Co in the elemental mapping data, it is reasonable to infer the product might be of cluster-mixed configuration. It has been proved theoretically and experimentally that core–shell configuration is preferred for the bimetallic nanocluster with large lattice mismatch, where the one with larger radius, higher cohesive energy and lower surface energy tend to segregate onto the surface.[32−34] In conjunction with the data of Au (with atomic radius of 1.44 Å, cohesive energy of −3.81 eV, surface energy of 1.17 J m^{-2}), obviously Co (with atomic radius of 1.26 Å, cohesive energy of −4.39 eV, surface energy of 1.5 J m^{-2}) incline to locate at the core of the clusters, similar with the prediction for Au–Ni and Ag–Ni system.[33,34] As for the absence of signals from Co in the XRD pattern, we believe heavy atom effect of Au and the overlap of the strongest diffraction of (111) of fcc-Co with (200) of fcc-Au as shown in Figure 2 might both make contribution. Similar phenomenon was also observed by Sun et al. in their report on Au@Fe_3O_4 core–shell structures,[35] where the diffractions from Fe_3O_4

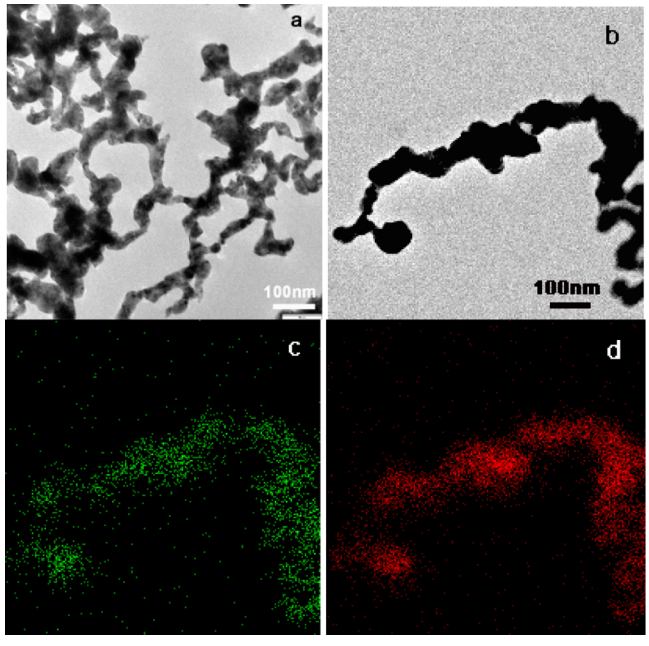

Figure 1. (a) Broad view TEM image, (b) bright-field image of a part of the chainlike nanostructures, (c, d) Au and Co element mapping data for the nanohybrid in part b.

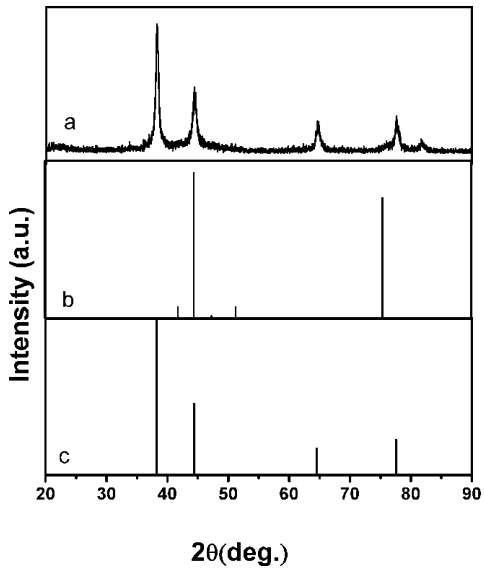

Figure 2. XRD pattern of (a) the as-prepared AuCo nanohybrids, (b, c) the standard pattern of fcc-Co with JCPDS No. 01–1259 and fcc-Au with JCPSD No. 04–0784, respectively.

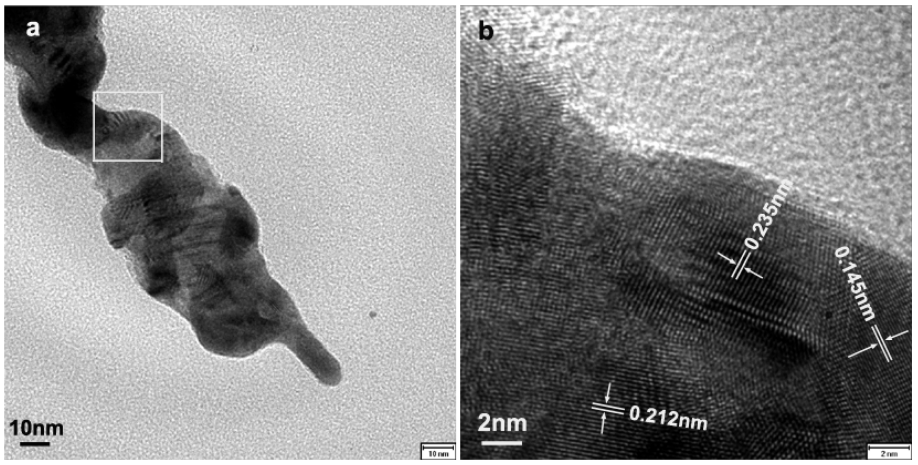

Figure 3. (a) High-magnification TEM image of part of the hybrids chain, (b) the corresponding HRTEM images recorded from the white frame in part a.

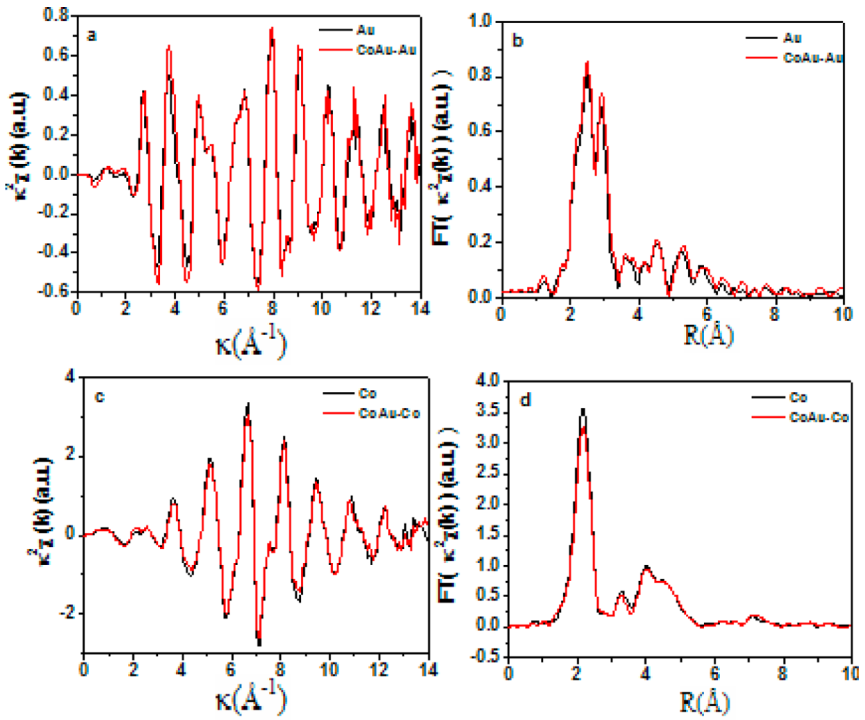

Figure 4. EXAFS $\kappa^2\chi(\kappa)$ functions and their Fourier transforms (FT) for the AuCo hybrid and the monometallic nanoparticles, respectively. (a, b) Co K-edge, (c, d) Au L-edge.

diminished with the increase thickness of Au shell. In this respects, the XRD results might further imply the Co-core/Au-shell cluster structure.

Figure 3a is a typical high-magnification TEM image recorded on part of the networklike structure. It reveals that there is sharp contrast over the structure, i.e., some area is brighter while some area is darker. Generally, the contrast difference in TEM image could be caused by the difference in component, thickness or space orientation. To address the essential factor causing the contrast difference in our case, we performed line scan elemental mapping at different parts of the same chain structure (see the Supporting Information, Figure S2). It reveals that the distribution of Au and Co is quite uniform in various areas. Thus, the difference in thickness and space orientation may be the major causes for the sharp contrast in the hybrids. Figure 3b is the corresponding high-resolution TEM (HRTEM) image recorded on the framed area in Figure 3a. The lattice fringes with space of 0.235 and 0.145 nm correspond with (111) and (220) facets of fcc-Au (JCPDS No. 04−0784), respectively, whereas the region with lattice fringe of 0.212 can be identified as cubic Co (JCPDS No. 01−1259). In addition, much dislocation is observable in the HRTEM image. The identification of the lattice from pure Au and pure Co further confirmed the cluster-mixed configuration.

To learn more structure and composition information, the Co K-edge and Au L_3-edge X-ray absorption fine structure (XAFS) spectra of Au−Co nanohybrids as well as that of Co and Au monometallic nanoparticles were measured. The XAFS data were analyzed by Feff8[36] software packages. The XAFS oscillations and their Fourier transform (FT) spectra of the AuCo nanohybrids and the monometallic nanoparticles are shown in Figure 4a, b (Co K-edge) and 4c, d (Au L_3-edge),

dx.doi.org/10.1021/am301572u | ACS Appl. Mater. Interfaces 2012, 4, 5643−5649

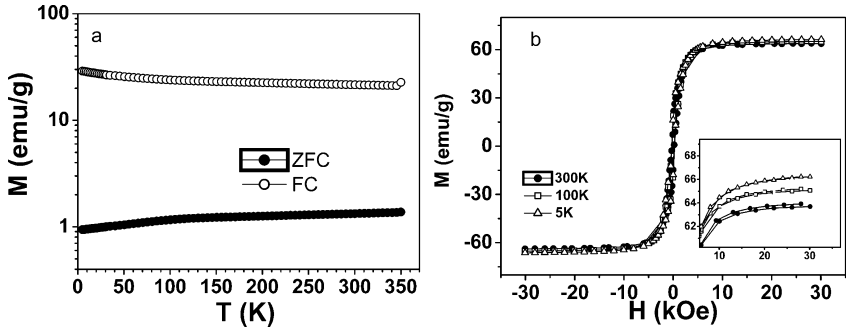

Figure 5. (a) FCM(T) and ZFCM(T) curves of the CoAu nanoalloys shown in a log-Y scale. (b) $M(H)$ curves measured at T = 5, 100, and 300 K. The upper left inset shows the open loops in the low-field region. The lower right inset reveals the saturation magnetization in high-field region.

respectively. Obviously, the signals originated from Au and Co can be both identified for the as-prepared product, which further confirms the Au−Co hybrid nature. The spectra also reveal that the peak positions of Au and Co in the AuCo sample are similar to those of the monometallic nanoparticles although the peak intensities for the former varied in some extent. No peaks related to Au−Co interatomic distances can be identified, which indicates Au−Au and Co−Co bonding dominated the hybrids, further excluding the possibility of intrametallic compound formation.

In addition to the information on the chemical bonding, the XAFS spectra can also give the signals on phase structure. Figure S3 in the Supporting Information shows the Co K-edge XANES spectra of AuCo hybrids and hcp-Co metallic foil. It can be seen that both the spectra exhibit four peaks as denoted by A, B, C, and D in order of increasing photon energy. The spectrum of AuCo hybrids deviates from that of Co foil in two aspects: (1) the intensity of peak B is slightly higher than that of peak C for AuCo hybrids, whereas it is vise versa for Co foil; (2) the energy separation of the B and D is larger for AuCo hybrids than Co foil. On the basis of the well-documented data,[37] the Co cluster in AuCo hybrids can be indexed as fcc structure. As discussed earlier, the Co-related diffraction cannot be well-identified in the XRD pattern of the hybrids. Then, we performed the experiment under similar reaction conditions but without the introduction of $HAuCl_4$ to get pure Co. As shown in Figure S4a in the Supporting Information, it displays five obvious features at 41.54, 44.23, 46.92, 50.80, and 75.76, respectively. For the XRD patterns of fcc- and hcp-Co (see Figure S4b, c in the Supporting Information), the major difference is the existence of a weak peak at around 51.2° for fcc-Co, which is absent for hcp-Co. Thus, the peak at 50.8° demonstrates its fcc structure. In addition, the relative peak intensity in Figure S4a in the Supporting Information is closer to the diffractions of fcc-Co. Thus, the XRD results might further evidence the fcc structure of the Co cluster in the hybrids. There are two stable phases for cobalt. The hexagonal close-packed (hcp) phase is stable for bulk at temperature below 450 °C, whereas fcc phase is stable above 450 °C and at room temperature for small particles.[38−40] The fcc structure of Co in our case indicated the small sizes of the cluster in the hybrids.

The magnetization measurements were performed by a SQUID magnetometer (Quantum Design) on a powder collection, ∼1.56 mg. The temperature dependent magnetizations, $M(T)$, were measured by the zero-field-cooling and field-cooling (ZFC and FC) modes from 5 to 350 K. For the ZFC measurement, the sample was cooled down to 5 K under zero applied field. Then, the data was collected in an applied field with H_{app} = 90 Oe, during the warming of the sample. For the FC curve, the data was also recorded in H_{app} = 90 Oe during the warming, however, with the sample cooled down to 5 K in the presence of a field of 10 kOe. Figure 5a shows the ZFCM(T) and FCM(T) curves in a log-Y scale to better reveal the behavior of the ZFCM(T) curve. Both curves demonstrate weak temperature dependency in the range of 5 to 350 K so that $\Delta M(T)$ = FCM(T)− ZFCM(T) does not decrease significantly with increasing temperature. It indicates that the magnetic anisotropy barrier is much larger than the thermal energy k_BT at T < 350 K. This is a feature different from that of pure Co micro/nanostructures, which show significant variation of magnetization in the same temperature range.[41−43]

The field-dependent magnetization, $M(H)$, curves of the as-prepared sample were also measured at T = 5, 100, and 300 K, respectively (Figure 4b). The coercivity is almost the same at these temperatures. This is consistent with the results of $M(T)$ measurements that $\Delta M(T)$ is almost temperature-independent. The inset on the lower right corner reveals the saturation behavior of the $M(H)$ curves in the high-ield region. The saturation magnetization, M_S, is then determined as 66.2, 65.2, and 63.9 emu/g at T = 5, 100, 300 K, respectively. The reduction in saturation magnetization from M_S(5K) to M_S(300K) accounts for only about 3.47%. This is consistent with the behavior of bulk Co, where the saturation magnetization decreases by only 1.03% from T = 5 to 300 K.[44,45] Similar behaviors have also been observed in submicrometer-sized Co hollow spheres and donut-shaped Co nanosprings.[41−43] By accounting for the atomic weight of Au and Co as 197.0 and 58.9, respectively, and assuming that the magnetic moments solely arise from the Co atoms, the average magnetic moment for each Co atom is then determined as 2.95 μ_B for each Co atom at T = 300 K. This is much higher than the corresponding bulk value of Co, ∼1.7 μ_B, and amazingly, approaches the value of an atomic Co, ∼3.0 μ_B. To date, this is the highest value ever reported for Co not in the form of an isolated atom. A clue for this enhancement may rely on the results by several different calculations that surface coating by noble metals (Au, Ag, Cu, Pd) over clusters of magnetic 3d elements (Fe, Co, Ni) could result in different electronic structures and thus induce large variations in the magnetic moments,[46−48] also agree with the prediction of the cluster mixed configuration of the nanohybrids. The FC loops loops performed at various temperatures as shown in Figure S5 in the Supporting Information reveal there is no exchange-biased effect observed. It indicates that hardly any oxidation occurred

Scheme 1. Illustration of the Formation Mechanism of the Chainlike AuCo Nanohybrids[a]

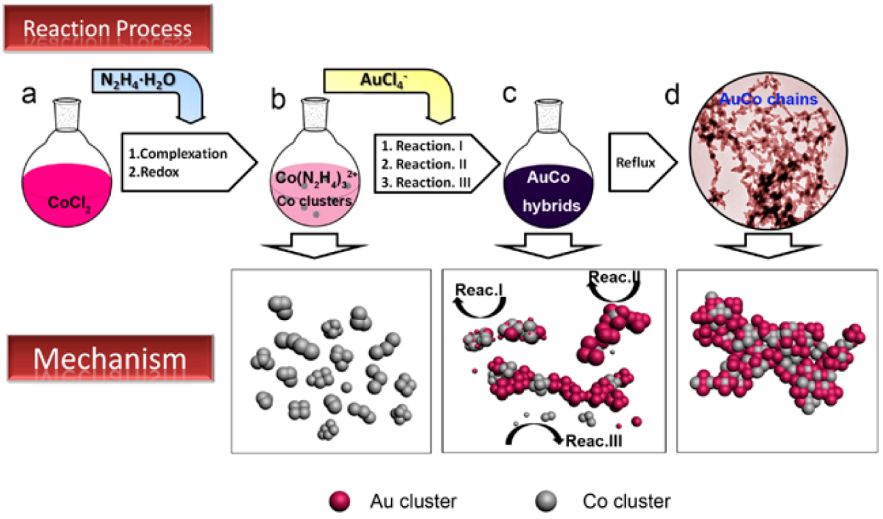

[a]The whole process can be briefly described as: (1) the complexation and redox reaction between $CoCl_2$ (a) and N_2H_4 H_2O, which produced $Co(N_2H_4)_3^{2+}$ and Co clusters (b), respectively; (2) after the introduction of $AuCl_4^-$ in the solution (b), three reactions happened simultaneously, i.e., the galvanic reaction between $AuCl_4^-$ and Co (React. 1), the redox reaction between $AuCl_4^-$ and N_2H_4 H_2O (React. 2), and the further reduction of the oxided Co^{2+} in reaction 1 by N_2H_4 H_2O (React. 3). It produced Au−Co hybrid clusters; (3) after refluxing, the reaction further proceeded and the hybrid clusters fused into chainlike structures because of the dipole−dipole interaction.

for Co, which might provide another evidence for the Co-core/Au-shell cluster configuration.

We believe that a sequential redox and an imperfection-promoted aggregation/diffusion process account for the formation of AuCo nanohybrids. As evidenced by our previous work,[41,43] the introduction of $N_2H_4.H_2O$ would both complex with Co^{2+} into $[Co(N_2H_4)_3]^{2+}$ and reduce Co^{2+} into metallic Co nanocrystals. When $HAuCl_4$ was added into the solution, on the one hand, galvanic reaction according to eq 1 is expected because of the large potential difference between Co^{2+}/Co (−0.277 V vs standard hydrogen electrode (SHE)) and $AuCl_4^-/Au$ (0.994 V vs SHE) redox pair; on the other hand, the redox reaction between $N_2H_4.H_2O$ and $AuCl_4^-$ also occurred as shown in eq 2. These redox processes led to the nucleation of metallic Au.

$$3Co + 2AuCl_4^- = 2Au + 3Co^{2+} + 8Cl^- \quad (1)$$

$$4AuCl_4^- + 3N_2H_4 = 4Au + 3N_2 + 12H^+ + 16Cl^- \quad (2)$$

Because $N_2H_4.H_2O$ is excessive in the reaction system, any Co that is oxidized into Co^{2+} during Au deposition will be reduced back to Co. The fast nucleation must generate much dislocation in both Au and Co nanoclusters. The high-energy states facilitated the aggregation and the subsequent diffusion of clusters with different composition, which eventually led to the formation of AuCo cluster mixed nanohybrids. The relative smaller radius, lower cohesive energy, and higher surface energy of Co than those of Au[32−34] might also benefit the diffusion of Co into the preformed Au nanoclusters. The dipole−dipole interaction among the bimetallic nanoparticles is believed to responsible for the formation of the chainlike structures, which is similar with the formation mechanism of Au nanochains as in our previous publications.[49] The whole process is illustrated in Scheme 1.

It was found that the molar ratio of $Co^{2+}/AuCl_4^{2-}$ is important for the uniform elemental distribution. When the molar ratio of $Co^{2+}/AuCl_4^{2-}$ is larger than 9:1, obvious phase segregation occurred. Figure S6 in Supporting Information gave typical TEM, HRTEM, and EDS data of the products obtained with the molar ratio of $AuCl_4^{2-}/Co^{2+}$ as 1:12. Panels b and c in Figure S6 in the Supporting Information are the HRTEM image and EDS data collected at the region of frame 1 in Figure S6a, whereas d and e in Figure S6 are the data corresponding to the region of frame 2, respectively. The adjacent lattice space is measured as 0.23 nm in Figure S6b in the Supporting Information, well-coincident with (111) plane of fcc-Au with JCPDS No. 04−0784. The lattice fringe distance in Figure S6d in the Supporting Information is 0.19 nm, in agreement with fcc-Co with JCPDS No. 01−1259. The corresponding EDS data demonstrated that region 1 is composed of nearly pure Au, whereas Co dominates region 2. We believe the similar nucleation rate of Au and Co is an important factor for the uniform elemental distribution. Once the redox kinectic balance is broken and the nuclei of either Au or Co grow into nanoparticles with larger size, heterogeneous junction rather than cluster-mixed structure would be preferred.

To verify the generality of the method, we also carried out the experiment under similar conditions but substituted $PtCl_6^{2-}$ for $AuCl_4^{2-}$. TEM observations reveal that chainlike nanostructures also dominate the products (see Figure S7 in the Supporting Information). EXAFS data (Figure S8 in the Supporting Information) indicate that unlike the phase-segregated component configuration in the AuCo nanohybrid, alloying occurred for CoPt nanohybrids. It is not difficult to understand because Co is miscible in Pt according to their phase diagram. Thus, the results suggest that the method might provide a new idea for the fabrication of bimetallic or mutimetallic nanohybrids with chainlike structures.

4. CONCLUSIONS

In this paper, the bulk immiscible metals, Au and Co, formed chainlike nanohybrids with uniform component distribution under mild conditions. A sequential redox and imperfection-promoted aggregation/diffusion process was proposed to

illustrate the formation mechanism of the nanohybrids and dipole−dipole interaction was believed to be responsible for the formation of chainlike structure. The products possess almost temperature-independent saturation magnetization from 5 to 300 K with the magnetic moment of each Co atom ~2.95 μ_B for each Co atom at 300 K, much higher than the bulk value (~1.7 μ_B) and approaching the theoretical value of an atomic Co (~3.0 μ_B). Control experiments indicate that the method is also efficient for the fabrication with chainlike CoPt nanoalloy. The synthetic strategy may provide a new idea for the controlled fabrication of bimetallic nanocrystals with interesting magnetic properties.

■ ASSOCIATED CONTENT

Supporting Information

More EDS, line-scan elemental mapping data, XANES spectra, FC loops of the AuCo nanohybrids, TEM image, EDS and EXAFS data of the CoPt chainlike structure, XRD pattern of pure Co. This material is available free of charge via the Internet at http://pubs.acs.org.

■ AUTHOR INFORMATION

Corresponding Author

*E-mail: guolin@buaa.edu.cn (L.G.); cpchen@pku.edu.cn (C.C.); wuzy@ustc.edu.cn (Z.-Y.W.).

Author Contributions

All authors have given approval to the final version of the manuscript.

Notes

The authors declare no competing financial interest.

■ ACKNOWLEDGMENTS

The authors are thankful for financial support from National Basic Research Program of China (2010CB934700), National Nature Science Foundation of China (21173015 & 20973019), and Weishi research Fund of Beihang (YWF-11-03-Q-085).

■ REFERENCES

(1) Ferrando, R.; Jellinek, J.; Johnston, R. L. *Chem. Rev.* **2008**, *108*, 845−910.
(2) Franceschi, S. D.; Kouwenhoven, L.; Schönenberger, C.; Wernsdorfer, W. *Nat. Nanotechnol.* **2010**, *5*, 703−711.
(3) Levin, C. S.; Hofmann, C.; Ali, A. T.; Kelly, A. T.; Morosan, E.; Nordlander, P.; Whitmire, K. H.; Halas, N. J. *ACS Nano* **2009**, *3*, 1379−1388.
(4) Fan, Z.; Shelton, M.; Singh, A. K.; Senapati, D.; Khan, S. A.; Ray, P. C. *ACS Nano* **2012**, *6*, 1065−1073.
(5) Cheng, K.; Sun, S. H. *Nano Today* **2010**, *5*, 183−196.
(6) Wang, L.; Zhang, J.; Meng, X. J.; Zheng, D. F.; Xiao, F. S. *Cata. Today* **2011**, *175*, 404−410.
(7) Lee, Y.; Garcia, M. A.; Huls, N. A. F.; Sun, S. H. *Angew. Chem., Int. Ed.* **2010**, *49*, 1271−1274.
(8) Thomas, K. G.; Kamat, P. V. *Acc. Chem. Res.* **2003**, *36*, 888−898.
(9) Shekhar, M.; Wang, J.; Lee, W. S.; Williams, W. D.; Kim, S. M.; Stach, E. A.; Miller, J. T.; Delgass, W. N.; Ribeiro, F. H. *J. Am. Chem. Soc.* **2012**, *134*, 4700−4708.
(10) Herzing, A. A.; Kiely, C. J.; Carley, A. F.; Landon, P.; Hutchings, G. J. *Science* **2008**, *321*, 1331−1335.
(11) Pompa, P. P.; Martiradonna, L.; Torre, A. D.; Sala, F. D.; Manna, L.; De Vittorio, M.; Calabi, F.; Cingolani, R.; Rinaldi, R. *Nat. Nanotechnol.* **2006**, *1*, 126−130.
(12) Kulakovich, O.; Strekal, N.; Yaroshevich, A.; Maskevich, S.; Gaponenko, S.; Nabiev, I.; Woggon, U.; Artemyev, M. *Nano Lett.* **2002**, *2*, 1449−1452.
(13) Lee, J. S.; Shevchenko, E. V.; Talapin, D. V. *J. Am. Chem. Soc.* **2008**, *130*, 9673−9675.
(14) Li, P.; Wei, Z.; Wu, T.; Peng, Q.; Li, Y. D. *J. Am. Chem. Soc.* **2011**, *133*, 5660−5663.
(15) Shaviv, E.; Banin, U. *ACS Nano* **2010**, *4*, 1529−1538.
(16) Enache, D. I.; Edwards, J. K.; Landon, P.; Solsona-Espriu, B.; Carley, A. F.; Herzing, A. A.; Watanabe, M.; Kiely, C. J.; Knight, D. W.; Hutchings, G. J. *Science* **2006**, *311*, 362−365.
(17) Ketchie, W. C.; Murayama, M.; Davis, R. J. *J. Catal.* **2007**, *250*, 264−273.
(18) Schrinner, M.; Proch, S.; Mei, Y.; Kempe, R.; Miyajima, N.; Ballauff, M. *Adv. Mater.* **2008**, *20*, 1928−1933.
(19) Liu, X. Y.; Wang, A. Q.; Li, L.; Zhang, T.; Mou, C. Y.; Lee, J. F. *J. Catal.* **2011**, *278*, 288−296.
(20) Guo, X. N.; Brault, P.; Zhi, G. J.; Caillard, A.; Jin, G. Q.; Coutanceau, C.; Baranton, S.; Guo, X. Y. *J. Phys. Chem. C* **2011**, *115*, 11240−11246.
(21) Zhang, H. J.; Watanabe, T.; Okumura, M.; Haruta, M.; Toshima, N. *Nat. Mater.* **2012**, *11*, 49−52.
(22) Lukanov, P.; Anuganti, V. K.; Krupskaya, Y.; Galibert, A. M.; Soula, B.; Tilmaciu, C.; Velders, A. H.; Klingeler, R.; Büchner, B.; Flahaut, E. *Adv. Funct. Mater.* **2011**, *21*, 3583−3588.
(23) Liong, M.; Lu, J.; Kovochich, M.; Xia, T.; Ruehm, S. G.; Nel, A. E.; Tamanoi, F.; Zink, J. I. *ACS Nano* **2008**, *2*, 889−896.
(24) Park, K.; Lee, S.; Kang, E.; Kim, K.; Choi, K.; Kwon, I. C. *Adv. Funct. Mater.* **2009**, *19*, 1553−1566.
(25) Gual, A.; Godard, C.; Castillón, S.; Curulla-Ferré, D.; Claver, C. *Cata. Today* **2012**, *183*, 154−171.
(26) Sumiyama, K.; Suzuki, K.; Makhlouf, S. A.; Wakoh, K.; Kamiyama, T.; Yamamuro, S.; Konno, T. J.; Xu, Y. F.; Sakurai, M.; Hihara, T. *J. Non-Cryst. Solids* **1995**, *192/193*, 539−545.
(27) Ferre, J.; Pénissard, G.; Marlière, C.; Renard, D.; Beauvillin, P.; Renard, J. P. *Appl. Phys. Lett.* **1990**, *56*, 1588−1590.
(28) Wang, D. S.; Li, Y. D. *J. Am. Chem. Soc.* **2010**, *132*, 6280−6281.
(29) Yan, J. M.; Zhang, X. B.; Akita, T.; Haruta, M.; Xu, Q. *J. Am. Chem. Soc.* **2010**, *132*, 5326−5327.
(30) Lu, Y.; Zhao, Y.; Yu, L.; Dong, L.; Shi, C.; Hu, M. J.; Xu, Y. J.; Wen, L. P.; Yu, S. H. *Adv. Mater.* **2010**, *22*, 1407−1411.
(31) Kong, Y.; Kong, L. T.; Liu, B. X. *J. Phys.: Condens. Matter* **2006**, *18*, 4345−4353.
(32) Gaudry, M.; Cottancin, E.; Pellarin, M.; Lermé, J.; Arnaud, L.; Huntzinger, J. R.; Vialle, J. L.; Broyer, M. *Phys. Rev. B* **2003**, *67*, 155409−1−155409−10.
(33) Rossi, G.; Rapallo, A.; Mottet, C.; Fortunelli, A.; Baletto, F.; Ferrando, R. *Phys. Rev. Lett.* **2004**, *93*, 105503−1−105503−4.
(34) Rapallo, A.; Rossi, G.; Ferrando, R.; Fortunelli, A.; Curley, B. C.; Lloyd, L. D.; Tarbuck, G. M.; Johnston, R. L. *J. Chem. Phys.* **2005**, *122*, 194308−1−194308−13.
(35) Xu, Z. C.; Hou, Y. L.; Sun, S. H. *J. Am. Chem. Soc.* **2007**, *129*, 8698−8699.
(36) Ankudinov, A. L.; Ravel, B.; Rehr, J. J.; Conradson, S. D. *Phys. Rev. B* **1998**, *58*, 7565−7576.
(37) Zhang, G. L.; Wu, Z. Y.; Li, A. G.; Wang, Y. S.; Zhang, J.; Abbas, M. L.; Hu, R.; Ni, X. B.; Tong, Y. P.; Hwu, Y. *Phys. Rev. B* **2004**, *69*, 115405−1−11504−4.
(38) Leslie-Pelecky, D. L.; Bonder, M.; Martin, T.; Kirkpatrick, E. M.; Liu, Y.; Zhang, X. Q.; Kim, S. H.; Rieke, R. D. *Chem. Mater.* **1998**, *10*, 3733−3736.
(39) Dupuis, V.; Tuaillon, J.; Prevel, B.; Perez, A.; Melinon, P.; Guiraud, G.; Parent, F.; Steren, L. B.; Morel, R.; Bartholemy, A.; Fert, A.; Mangin, S.; Thomas, L.; Wernsdorfer, W.; Barbara, B. *J. Magn. Magn. Mater.* **1997**, *165*, 42−45.
(40) Owen, E. A.; Jones, D. M. *Proc. Phys. Soc. B* **1954**, *67*, 456−466.
(41) Guo, L.; Liang, F.; Wang, N.; Kong, D. S.; Wang, S. M.; He, L.; Chen, C. P.; Meng, X. M.; Wu, Z. Y. *Chem. Mater.* **2008**, *20*, 5163−5168.
(42) He, L.; Chen, C. P.; Liang, F.; Wang, N.; Guo, L. *Phys. Rev. B* **2007**, *75*, 214418−1−214418−4.

(43) Guo, L.; Liang, F.; Wen, X. G.; Yang, S. H.; He, L.; Zheng, W. Z.; Chen, C. P.; Zhong, Q. P. *Adv. Funct. Mater.* **2007**, *17*, 425−430.
(44) Kuz'min, M. D. *Phys. Rev. Lett.* **2005**, *94*, 107204−1−107204−4.
(45) Kuz'min, M. D.; Richter, M.; Yaresko, A. N. *Phys. Rev. B* **2006**, *73*, 100401(R)-1−100401(R)-4.
(46) Guevara, J.; Llois, A. M.; Weissmann, M. *Phys. Rev. Lett.* **1998**, *81*, 5306−5309.
(47) Sun, Q.; Kandalam, A. K.; Wang, Q.; Jena, P.; Kawazoe, Y.; Marquez, M. *Phys. Rev. B* **2006**, *73*, 134409−1−134409−6.
(48) Wang, Q.; Sun, Q.; Yu, J. Z.; Hashi, Y.; Kawazoe, Y. *Phys. Lett. A* **2000**, *267*, 394−402.
(49) Zhang, D. F.; Niu, L. Y.; Jiang, L.; Yin, P. G.; Sun, L. D.; Zhang, H.; Zhang, R.; Guo, L.; Yan, C. H. *J. Phys. Chem. C* **2008**, *112*, 16011−16016.